Mesoporous NiFe$_2$O$_4$ with Tunable Pore Morphology for Electrocatalytic Water Oxidation

Christopher Simon,[a] Jana Timm,[a] David Tetzlaff,[b, c] Jonas Jungmann,[a] Ulf-Peter Apfel,*[b, c] and Roland Marschall*[a]

Mesoporous NiFe$_2$O$_4$ for electrocatalytic water splitting was prepared via soft-templating using citric-acid-complexed metal nitrates as precursors. The mesopore evolution during thermal treatment was examined systematically giving insights into the formation process of mesoporous NiFe$_2$O$_4$. Detailed nitrogen physisorption analysis including desorption scanning experiments reveal the presence of highly accessible mesopores generating surface areas of up to 200 m^2/g. The ability of the

NiFe$_2$O$_4$ powders to perform electrocatalytic oxygen evolution reaction under alkaline conditions was investigated, highlighting the advantages of mesopore insertion. The most active samples reach a current density of 10 mA cm^{-2} at an overpotential of 410 mV with a small Tafel slope of 50 mV dec^{-1}, indicating an enhanced activity that originated from the increased catalyst surface.

1. Introduction

Electrocatalytic water splitting using renewable energies to form green hydrogen and oxygen has attracted a widespread interest to replace fossil fuels as major energy carrier. Currently, the oxygen evolution half reaction (OER) is regarded to be the major bottle-neck of water splitting due to its hampered kinetics involving a multi-step proton and electron transfer. Noble metal electrocatalysts, such as RuO$_2$ and IrO$_2$ are widely used for OER, however, their prohibitive scarcity and cost limit their potential widespread use in electrolyzers. Therefore, researchers have focused on first-row transitions metal oxides like Co$_x$O$_y$,[1,2] Mn$_x$O$_y$,[3,4] Fe$_x$O$_y$,[5,6] Ni$_x$O$_y$,[7,8] and combinations thereof[9–11] as potential electrocatalysts for OER.

Among the multiple transition metal oxides, ferrites with the general formula M^{II}Fe$_2$O$_4$ (M=Ca, Zn, Mg, Ni, Co, Mn etc.) have gained considerable attention due to their compositions made up from earth-abundant elements and widespread application fields besides electrocatalysis[12–15] in gas

sensing,[16,17] and photocatalysis/photoelectrochemistry.[18–27] Especially nickel ferrite has been considered as efficient OER electrocatalyst, with outstanding high stability in alkaline media, excellent redox properties, and ferromagnetism facilitating the catalyst separation from solution.[28,29] Already in 1999, N. K. Singh and R. N. Singh showed that the inverse spinel NiFe$_2$O$_4$ is a highly active material in the electrocatalytic water oxidation with an overpotential of 379 mV at a current density of 100 mA cm^{-2}, which outcompetes pure iron oxide (spinel Fe$_3$O$_4$).[30]

A common approach to optimize the performance of an electrocatalyst is based on the preparation of materials with high surface-to-volume ratio by means of nano-/mesostructuring.[31,32] Such porous structures provide large accessible active surface areas, and mass transport characteristics can be tailored. However, downsizing the pore size and therefore increasing the surface area limits the rate of mass transport of reactants and products influencing the overall performance. Likewise, ordering of the pores can influence mass transport characteristics during this type of reactions, too.[33] Due to the variety of parameters influencing the formation and activity of mesoporous electrocatalysts, detailed studies are necessary to understand the structure/activity relationships of mesoporous electrocatalysts.[34] Since many transition metal oxides are intrinsically poorly conductive,[35,36] shortening the diffusion pathways by nano-/mesostructuring can improve the transport of charge carriers through the material.

Various mesoporous NiFe$_2$O$_4$ were described in literature. For example, Haetge et al. reported a soft-templating route to prepare ordered mesoporous NiFe$_2$O$_4$ thin films with pore widths of around 16 nm, using a non-commercial KLE polymer (poly(ethylene-co-butylene)-b-poly(ethylene oxide) diblock copolymer[37]) for pseudocapacitive charge storage.[38] Jia et al. used a similar soft-templating approach based on the commercial Pluronic® P-123 block copolymer to synthesize non-ordered

[a]   C. Simon, Dr. J. Timm, J. Jungmann, Prof. R. Marschall
      Department of Chemistry
      University of Bayreuth
      Universitaetsstrasse 30, 95447 Bayreuth, Germany
      E-mail: roland.marschall@uni-bayreuth.de
[b]   D. Tetzlaff, Prof. U.-P. Apfel
      Inorganic Chemistry I – Bioinorganic Chemistry
      Ruhr-University Bochum
      Universitaetsstrasse 150, 44801 Bochum, Germany
[c]   D. Tetzlaff, Prof. U.-P. Apfel
      Fraunhofer Institute for Environmental, Safety, and Energy Technology
      Osterfelder Strasse 3, 46047 Oberhausen, Germany
      E-mail: ulf-peter.apfel@umsicht.fraunhofer.de

ChemElectroChem

Articles
doi.org/10.1002/celc.202001280

Chemistry Europe
European Chemical
Societies Publishing

mesoporous $NiFe_2O_4$ powders for acetone detection with two major types of pores with 7 and 33 nm in diameter.[39]

Further, Gu *et al.*, Li *et al.*, and Yen *et al.* reported on ordered mesoporous $NiFe_2O_4$ (pore diameters of 7 nm, 5–25 nm, and 3–8 nm), which can be used as microwave adsorber material or bifunctional catalyst for Li-O_2 batteries. Here, the generation of the ordered mesoporous structures was based on a multi-step hard-templating strategy (nanocasting) using mesoporous silica (KIT-6, SBA-15, MCM-48) as template, which can be a time-consuming synthesis and leaves residual silica in the material.[40–42]

To avoid the disadvantages of having tedious polymer synthesis or impurities of insulating SiO_2, we herein focused on a simple, rapid, one-step soft-templating route, based on the evaporation-induced self-assembly process (EISA) using the commercially available triblock copolymer Pluronic® (P-123) and citric acid, to synthesize ordered mesoporous phase-pure $NiFe_2O_4$ powders with tunable pore sizes in the range of 5–12 nm for application in electrocatalytic oxygen evolution reaction. The porosity, pore accessibility, phase composition and crystallinity of the powders were tuned by the calcination temperature, giving insights into the importance of these parameters for application. Detailed morphological investigations including nitrogen physisorption, electron microscopy, and X-ray diffraction were performed to understand the results from electrocatalytic water oxidation studies, which reveal the influence of accessible surface area, connected pores, and crystallinity on the overall activity.

2. Results and Discussion

Micelle-templated ordered mesoporous transition metal oxides, and carbonates as their intermediates during thermal treatment, are known to be easily available *via* the formation of metal complexes with citric acid.[31,43] Therefore, this approach was followed to prepare the mixed metal oxide $NiFe_2O_4$ with highly homogeneous mesopores here by using Pluronic P-123® (P-123) with citric acid calcined at various temperatures (275 °C, 400 °C, 450 °C, 550 °C). For comparison, samples were also prepared using only P-123 and only citric acid as templates, to reveal their influence on the pore generation and activity.

The mesoporous structure of $NiFe_2O_4$ is largely affected by the calcination temperature and the synthesis conditions, in general. The concentrations of P-123 (0.03 equivalents concerning the Ni precursor) and citric acid (4.3 equivalents concerning the Ni precursor) were kept constant in order to stay well below the critical micelle concentration (cmc) before the solvent evaporation step, and to investigate the role of the templating/chelating agents and the calcination temperature. To understand the occurring processes and to investigate mesopore evolution during the synthesis in detail, we performed thermogravimetric analysis coupled with online mass spectrometry (TG-MS) with as-synthesized samples before calcination (Figure 1). Pristine P-123 shows the highest mass loss between 200 and 350 °C with maxima of the CO_2 and H_2O MS traces at 334 °C, while nickel iron oxide samples prepared only with P-123 start decomposing already at 87 °C and show then a slow decay ending at 358 °C. The corresponding CO_2 and H_2O MS traces show therefore a broad distribution in the temperature range between 87 °C and 358 °C with no distinguishable maxima. The difference in the decomposition decays of pristine P-123 and the hybrids can be explained by the different decomposition steps of precursors iron(III) nitrate and nickel(II) nitrate. Here, the decomposition of both nitrate salts is quite complex and takes place in several stages via metastable intermediates like $Ni(NO_3)_{1.5}O_{0.25} \cdot H_2O$ or $Fe_4O_4(OH)_2(NO_3)_2 \cdot 2H_2O$.[44,45]

The TG curve of a nickel iron oxide sample prepared only with citric acid shows a mass loss at 130–153 °C that can be
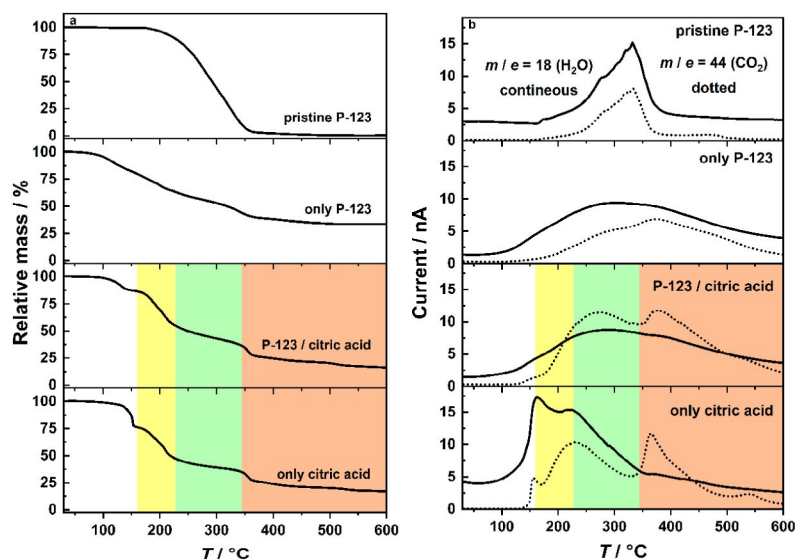

Figure 1. a) TG measurements of as-prepared $NiFe_2O_4$ samples and the pristine P-123, b) H_2O ($m/e = 18$, continuous lines) and CO_2 ($m/e = 44$, dotted lines) evolution during TG analysis monitored *via* mass spectrometry.

ChemElectroChem

Articles
doi.org/10.1002/celc.202001280

**Chemistry
Europe**
European Chemical
Societies Publishing

assigned to the loss of surface-adsorbed water, and further to a partial decomposition of citric acid, which is confirmed by the signals in the corresponding mass spectra of H_2O and CO_2 at 156/162 °C, respectively. In this case, synthesis only with citric acid, the CO_2 MS trace must result from the partial decomposition of citric acid due to the absence of any other carbon source. The 2nd decomposition step at 173–226 °C marks the decomposition of the precursor complex into intermediate carbonate species (yellow zone in Figure 1), as explained below. The 3rd decomposition step at 343–363 °C can be assigned to the transformation of these carbonates into the metal oxide (red zone in Figure 1), causing a prominent peak in the CO_2 MS trace at 364 °C, while a peak in the H_2O MS trace is missing at this temperature. Bernicke et al. observed a similar behavior during the citric acid-supported templating strategy of mesoporous NiO thin films.[31]

The two decomposition steps at 173–226 °C and 343–363 °C are separated by a plateau. Stable amorphous carbonate intermediates like $NiCO_3$ might be present at this temperature range (green zone in Figure 1).[31] Combination of P-123/citric acid results in a similar TG curve, compared to the TG curve of samples prepared only with citric acid, indicating the presence of intermediate carbonate species. According to the results from TG analysis, carbonates may be present between ~230 °C and ~340 °C. Furthermore, the presence of amorphous carbonates can facilitate polymer removal without sintering of pore walls.[43]

To check the presence and amorphous nature of intermediate carbonate species, as-synthesized samples were calcined at 275 °C and investigated using Cu PXRD and DRIFT spectroscopy. PXRD patterns of samples calcined at 275 °C show no reflections indicating crystalline phases (dotted line, Figure 2a). For all samples calcined at 275 °C, a prominent double peak at 1600–1400 cm^{-1} is present in the DRIFT spectra indicating carbonate anions (Figure S1).[43,46,47] When calcining these samples at 400 °C or above, no IR bands belonging to carbonate anion vibrations are present anymore, which is in agreement with the results from TG-MS analysis. Additionally, at calcination temper-

ature 400 °C or higher an IR signal at 3699 cm^{-1} is detectable and can be attributed to O—H vibrations of isolated O—H groups on metal oxide surfaces.[48] This vibration is only IR active if no or weak hydrogen bridge bonds are present in the material. P-123 is a polar block copolymer with O—H and ether bounds, which could form strong hydrogen bridge bonds with O—H groups on the metal oxide surface.[49,50] Therefore, the appearance of the IR signal at 3699 cm^{-1} can be correlated to the complete removal of P-123. TG-MS analysis and IR spectroscopy demonstrate the role of citric acid as carbonate source in the presented synthesis. These amorphous carbonates are stable in a relatively wide temperature range of 226–343 °C.

PXRD patterns are shown in Figure 2a. As expected and in accordance with literature data,[51] the $NiFe_2O_4$ samples crystallize between 400 °C and 550 °C, which is indicated by the rise of reflections at 450 °C and especially 550 °C. In this temperature range, the carbonates are already decomposed. PXRD patterns indicate the presence of single-phase, nanocrystalline $NiFe_2O_4$ when citric acid is present during the synthesis. All reflections can be indexed according to the $NiFe_2O_4$ reference pattern (ICOD, no. 00-044-1485). In contrast, samples prepared only with P-123 without citric acid are not completely phase-pure. The impurity identified from PXRD is hematite (α-Fe_2O_3), as marked in Figure 2a.[52] SAED patterns (Figure S2) further confirm these findings. Citric acid might act as chelating agent of the cations, also preventing phase separation.[53] This finding goes in line with a decreased Ni:Fe ratio below the optimum value of 0.5 (Figure S3), which can be detected via EDXS for samples prepared only with P-123. Even the errors for the EDXS data of the prepared only with P-123 are remarkably higher compared to the samples where citric acid was used. These findings go in line with the already mentioned phase impurity of the samples only prepared with P-123.

For samples prepared at 550 °C, calculated averaged crystallite sizes L_{hkl} from the integral width of the (220), (400), (511) and (440) reflections are 7.6 ± 0.6 nm (sample prepared only with P-123), 12.0 ± 0.7 nm (sample prepared only with
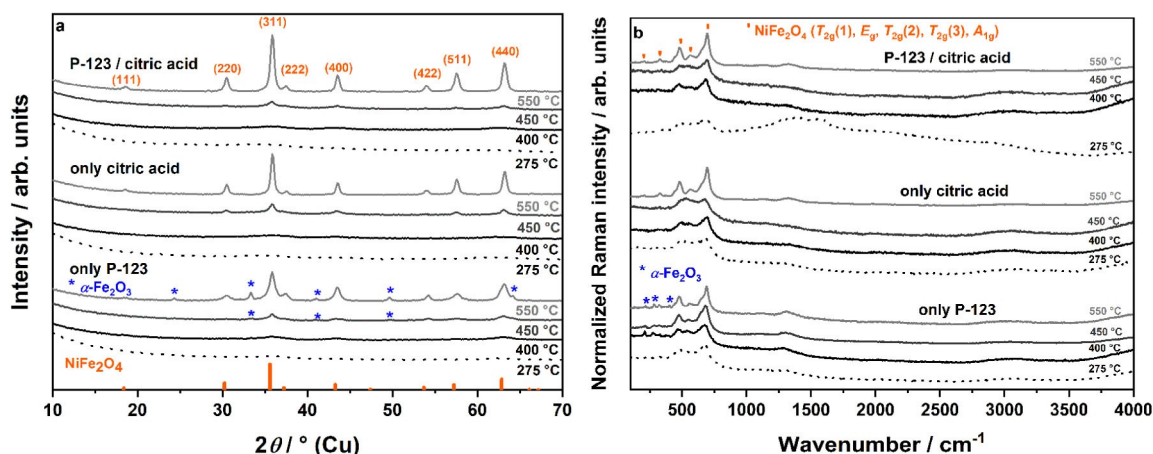

Figure 2. a) Cu PXRD patterns and b) Raman spectra of mesoporous $NiFe_2O_4$ samples calcined at 275 °C, 400 °C, 450 °C, and 550 °C. Samples were prepared only with P-123, only with citric acid, and with P-123 plus citric acid combined.

ChemElectroChem

Articles
doi.org/10.1002/celc.202001280

Chemistry Europe
European Chemical
Societies Publishing

citric acid), and 10.6 ± 0.6 nm (sample prepared with P-123/citric acid).
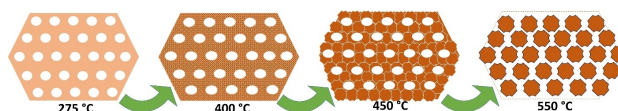
Phase-purity was also checked by Raman spectroscopy, especially to exclude the presence of hematite by-phases, since small amounts of hematite in spinel nanocrystals might not be detected by PXRD. For cubic spinels with $Fd\bar{3}m$ space group, five Raman active lattice modes were expected: A_{1g} (691 cm^{-1}) $+ E_g$ (332 cm^{-1}) $+ 3$ T_{2g} (201 cm^{-1}, 487 cm^{-1}, 570 cm^{-1}).[54–57] The A_{1g} signal corresponds to the symmetric stretching mode of M—O bonds in tetrahedral units. The $T_{2g}(2)$ and $T_{2g}(3)$ signals can be assigned to the asymmetric stretching mode and to the asymmetric bending of M—O bonds in octahedral units, respectively. The E_g and $T_{2g}(1)$ signals match with the symmetric bending and stretching modes of metal oxygen bonds, also located in octahedral voids. In contrast, trigonal hematite (space group $R\bar{3}c$) exhibits seven active lines in the Raman spectrum: $2 A_{1g}$ (225 cm^{-1}, 498 cm^{-1}) $+ 5 E_g$ (247 cm^{-1}, 293 cm^{-1}, 299 cm^{-1}, 412 cm^{-1}, 613 cm^{-1}).[58] Thus, spinel-type $NiFe_2O_4$ and trigonal hematite can clearly be distinguished by their Raman profiles. As presented in Figure 2b, the Raman modes of $NiFe_2O_4$ are present for all samples calcined at 550 °C. Additionally, the Raman spectrum of sample prepared only with P-123 additionally features prominent signals of hematite, including the intense signal at 293/299 cm^{-1}. Typically, the materials calcined at lower temperature suffer from a lack of crystallinity, thereby signal intensity decreases. However, the most intense $T_{2g}(2)$ and A_{1g} modes are visible in all Raman spectra. Occurring signals at 1100–1500 cm^{-1} can be interpreted as 2nd order peaks.[59] No signals of crystalline or amorphous carbonate species could be detected by this technique. Raman spectroscopy supported the results obtained from PXRD, pointing out that the addition of citric acid as chelating agent is mandatory to get pure $NiFe_2O_4$ materials. However, due to the small crystallites and therefore only poor Raman intensities, quantification of the occupancy of the tetrahedral and octahedral sites is not reliable.

Additionally, ^{57}Fe Mössbauer spectra of samples calcined at 550 °C, taken at ambient temperature, are presented in Figure S4. Isomer shifts (δ) of 0.32 mm/s (only citric acid, Figure S4b) and 0.25 mm/s (P-123/citric acid, Figure S4c) exhibit the presence of Fe(III) cations in two different local surroundings in the $NiFe_2O_4$ lattice. Ferric cations are coordinated tetrahedral or octahedral by oxygen anions, respectively. For those phase-pure samples, the observed sextets (hyperfine splitting) are typical of Fe cations in a permanent magnetic state. Detailed analysis display the presence of two overlapping sextets, corresponding to two iron sites. The inversion parameter X can be estimated by fitting both sextets separately.[61,62] Resulting values of 0.68 (only citric acid) and 0.35 (P-123/citric acid) indicate the presence of a partially inverse spinel. However, Agouriane et al. have postulated a value of $X = 0.95$–0.97 for $NiFe_2O_4$, determined by Rietveld refinement and Mössbauer spectroscopy. The significant deviations may originate from the different calcination temperature (1000 °C vs. 550 °C), since the calcination temperature and therefore crystallinity can have a major influence on the inversion parameter.[63,64] For sample prepared only with P-123, a third iron site is present since the sample is a phase mixture of

$NiFe_2O_4$ and α-Fe_2O_3. To exclude the impact of P-123 on the formation of phase mixtures of $NiFe_2O_4$ and α-Fe_2O_3, we investigated samples in which no P-123 and no citric acid was used in the synthesis, and we find the same phase mixture of $NiFe_2O_4$ and α-Fe_2O_3 after calcination (Figure S5). Due to phase-impurities, samples prepared only with P-123 and without P-123/without citric acid will thus no longer be discussed in the following. To summarize, the phase-purity of samples prepared with citric acid as chelating agent is proven by PXRD, SAED, Raman spectroscopy, EDXS, and Mössbauer spectroscopy. The chelation of metal cations with citric acid ensures their uniform distributions, preventing phase separation successfully.

TEM images and SEM images of mesoporous $NiFe_2O_4$ samples are shown in Figure 3 and Figure S5 and S6, respectively. Generally, both TEM and SEM images show big agglomerates in the μm size range, which are characterized by sub-structures in the nm size range. The SEM images of the sample only with citric acid (Figure S6) and the sample with P-123 and citric acid (Figure S7) show nanosized spherical particles as sub-structures. Nevertheless, these sub-structures can be better resolved using TEM analysis, allowing detailed analysis of the generated morphology. TEM image of sample prepared only citric acid and calcined at 275 °C (Figure 3a) clearly demonstrates a bulk material with regularly changing material contrast, verifying a high porosity even at 275 °C. If the P-123 polymer is additionally used in the synthesis combined with citric acid (P-123/citric acid), the brighter spots are more pronounced, showing that the P-123 possibly still blocks the pores at 275 °C (Figure 3e). Increasing the temperature to 400 °C affects the transformation of the amorphous carbonates to the amorphous metal oxide (cf. Figure 2). The morphology of the sample with only citric acid is completely conserved at 400 °C (Figure 3b). For the sample prepared with P-123/citric acid, the voids can now be interpreted as mesopores, since the P-123 is decomposed (Figure 3f). At 450 °C, the crystallization of $NiFe_2O_4$ starts, but samples maintain their remarkable porosities (Figure 3c,g). Interestingly, morphologies of samples only with citric acid and P-123/citric acid do not distinguish significantly at 400 °C and 450 °C, showing non-ordered mesopores. This indicates that the porosity is also introduced by the use of citric acid, not solely by the P-123. At 550 °C (Figure 3 d,h), the morphologies have changed to nanoparticular structures with interparticular pores between singular nanoparticles (Scheme 1).

According to the results from PXRD, initial crystal growth occurs in this temperature range (450–550 °C), causing morphological transformations. When the synthesis is performed only with citric acid, particles with a size of (21.0 ± 4.1) nm can be observed. However, the particles are strongly agglomerated,

Scheme 1. Morphological transformation of mesoporous $NiFe_2O_4$ upon annealing.

ChemElectroChem

Articles
doi.org/10.1002/celc.202001280

**Chemistry
Europe**
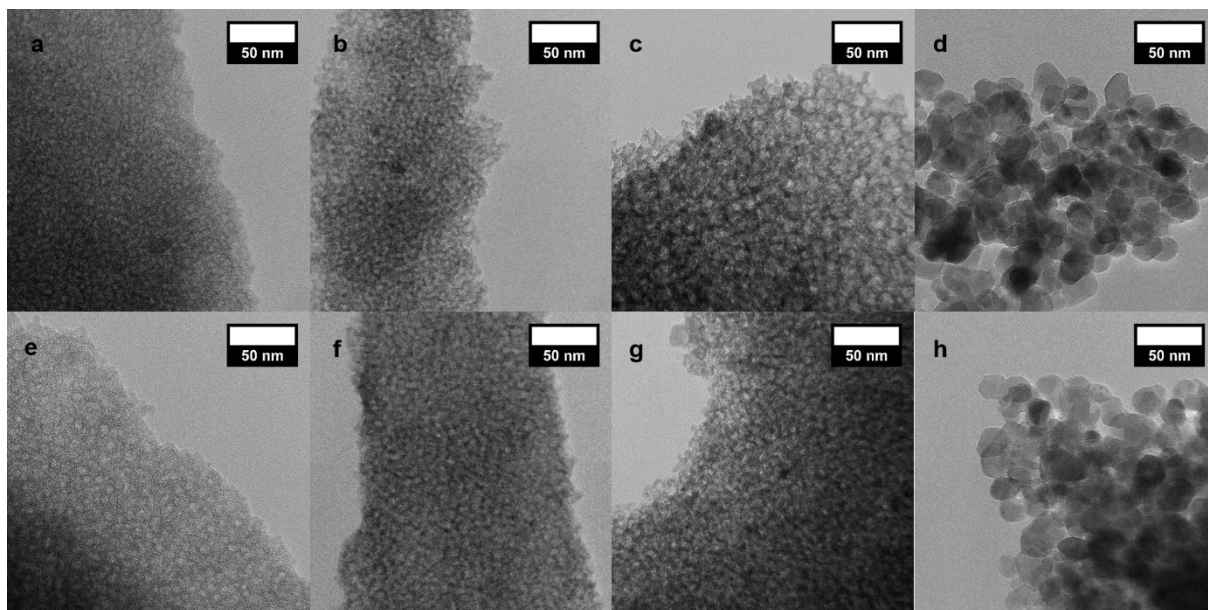
European Chemical
Societies Publishing

Figure 3. TEM images of mesoporous NiFe$_2$O$_4$ samples prepared only with citric acid calcined at 275 °C (a), 400 °C (b), 450 °C (c), and 550 °C (d). TEM images of mesoporous NiFe$_2$O$_4$ samples prepared with P-123/citric acid calcined at 275 °C (e), 400 °C (f), 450 °C (g), and 550 °C (h).

which impedes accurate particles size estimation. When P-123 and citric acid are combined in the synthesis, particles of a relatively uniform spherical shape with diameters of around (14.3 ± 2.4) nm are observed. The particle sizes are also slightly larger than the calculated crystallite sizes from PXRD. In general, NiFe$_2$O$_4$ tends to form a particular nanosized structure at 550 °C. The addition of P-123 further seem to inhibit the particle growth, resulting in different particle sizes at a calcination temperature of 550 °C (14.3 nm vs. 21.0 nm).

Detailed physisorption studies were performed to reveal the evolution of mesopores during the synthesis of NiFe$_2$O$_4$ (Figure 4). In Figure 4, the nitrogen physisorption isotherms of the mesoporous NiFe$_2$O$_4$ samples prepared under various conditions are shown. The corresponding pore size distributions and cumulative pore volumes are presented in Figure 4. The analyzed data of the nitrogen physisorption measurements are summarized in Table 1.

Physisorption isotherms show hysteresis loops clearly indicating the presence of mesopores in each prepared sample (type 4(a) isotherms, *cf.* Table 1).[65] The shape and starting p/p_0 values of the hysteresis of the physisorption isotherms differ depending on the synthesis conditions, indicating a morpho-

logical transformation in the relevant temperature range. The isotherms of the samples which were calcined only at 275 °C show already hysteresis loops indicating mesopores. The adsorption and the desorption isotherm branches of the samples prepared with P-123/citric acid are not overlapping at low relative pressure in contrast to isotherm branches of the samples without P-123 (only citric acid). This effect can be attributed to polymer residues due to swelling processes and irreversible nitrogen adsorption.[66] The specific surface area of the sample prepared with P-123/citric acid is only 53 m^{2}g^{-1}, while the sample prepared only with citric acids exhibits a specific surface area of 285 m^{2}g^{-1}. Residuals of P-123, which are present at 275 °C (*cf.* TG-MS and TEM analysis (Figure 1, Figure 3b)) inhibit the accessibility of the pores/ sample surface for nitrogen gas molecules and lead therefore to lower surface areas and also decreased pore volumes compared to the samples prepared only with citric acid (0.05 cm^{3}g^{-1} *vs.* 0.28 cm^{3}g^{-1}). It confirms that the loss of carbonate species due to citrate addition already leads to a highly porous mesostructure. This could be further proven by the analysis of the pore sizes. Both samples with/without P-123 (P-123/citric acid and only citric acid) are already mesoporous with narrow pore size

Table 1. Results obtained from nitrogen physisorption measurements presented in Figure 4. The averaged values of three different samples and the standard deviation are presented in Table S3.

	Only citric acid				P-123/citric acid			
	275 °C	400 °C	450 °C	550 °C	275 °C	400 °C	450 °C	550 °C
Surface area [m^{2}g^{-1}]	285	220	208	44	53	190	202	67
Pore width [nm]	5.0	5.0	5.1	12.0	4.6	6.0	5.1	10.0
Pore volume [cm^{3}g^{-1}]	0.28	0.27	0.24	0.13	0.05	0.31	0.22	0.15

ChemElectroChem

Articles
doi.org/10.1002/celc.202001280

Chemistry Europe
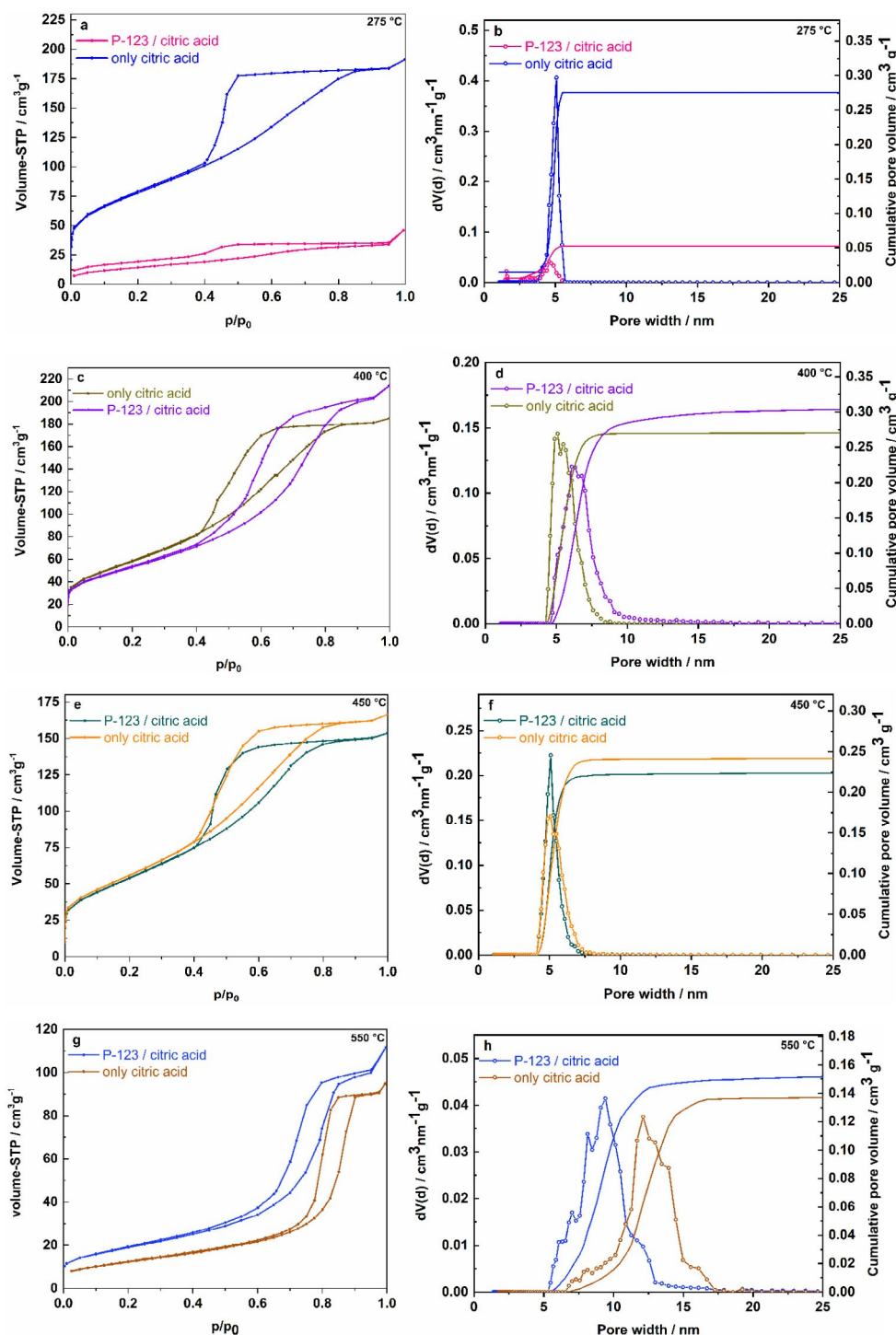European Chemical
Societies Publishing

Figure 4. a, c, e, g) N_2 physisorption isotherms of samples calcined at 275 °C, 400 °C, 450 °C and 550 °C, respectively, and b, d, f, h) corresponding pore size distributions plus cumulative pore volumes (obtained by NLDFT analysis).

distribution with maxima at 4.6 nm and resp. 5.0 nm, but the pore volume is much larger when only citric acid is used. In summary, the highly mesoporous morphology of amorphous $NiFe_2O_4$ can already be gained by the usage of citric acid.

At higher calcination temperature the P-123 residues are removed, and therefore the specific surface area of the samples prepared with/without P-123 (P-123/citric acid and only citric

acid) approach each other. Samples calcined at 400 °C and 450 °C have very high specific surface area of around 200 $m^2 g^{-1}$. Furthermore, the pore size distributions are very narrow. As already observed by TEM analysis, morphologies of both types of samples are quite similar at this temperature range (*cf.* Figure 3b,c,f,g). Despite the non-ordered porosity found in TEM images, the pore sizes achieved are highly

ChemElectroChem

Articles
doi.org/10.1002/celc.202001280

Chemistry Europe
European Chemical
Societies Publishing

homogeneous at this temperature treatment, peaking at 5–6 nm. At a calcination temperature of 550 °C, the templated-like morphology transform to a nanoparticular structure, as indicated by PXRD and TEM analysis (cf. Figure 2a and Figure 3d,h). These particles also form interparticular voids, which could be detected in the mesoporous range via nitrogen physisorption. The sample prepared only with citric acid exhibits larger pores than the sample with P-123/citric acid combined (12 nm vs. 10 nm), which can be correlated to larger particles seen in TEM images.

To further underline the relation between the crystallization and the porosity of the materials, samples with citric acid and P-123 were calcined to temperature up to 800 °C (Figure S7). The maxima of the pore size distribution of these samples shift towards larger pores (see Table S1), and the pore size distribution gets broader with increasing calcination temperatures (Figure S7). The higher calcination temperature promotes the transformation of smaller mesopores into larger but more non-ordered mesopores due to crystallite growth, as can be seen in the broadening of the pore size distribution (Figure 4). As a result, surface areas decrease strongly with increasing median pore size in all cases (cf. Table 1).

To further investigate the influence of the different calcination temperatures, the varying shapes of the hysteresis loops of the nitrogen physisorption isotherms due to modified mesoporosity were investigated via hysteresis scans. This method can unfold the pore connectivity of mesopores in a material, and therefore the origin of the mesopores of the different samples can be revealed. The pore connectivity is a very important property of functional porous materials for transport-related applications, e.g. electrocatalytic water oxidation. Additionally, the detection of different pore systems in one material is possible by this method.[67]

The desorption scanning method was used to investigate the desorption behavior of the pores in dependence of the neighboring pores. In general, if the desorption behavior of pores is dependent on the neighboring pore and the pore filling grade, the desorption of different isotherm desorption scans intersect in only one point at the p/p_0 value of the start/end of the hysteresis. If the desorption behavior of the pores is independent of the neighboring pores and the pore filling, the desorption of different isotherm scans shows hysteresis curves comparable to each other. Furthermore, the pore size distribution resulting from the different scans is comparable to each other.[68] For the desorption scanning isotherms, the adsorption was only run to a particular p/p_0 value in every cycle, and the desorption characteristics of the sample were detected. In Figure 5a,c,e, the hysteresis scans of samples prepared only with citric acid and calcined at different temperatures are presented. The first scan was measured over the whole range of p/p_0 up to 0.995 (cf. Figure 4). The other maximum adsorption points were chosen due to the hysteresis occurring in this range. The measured desorption branch of all scanning isotherms was then analyzed concerning the pore size distribution via NLDFT method (Figure 5b,d,f). In Figure 5b and d, the analyzed data of the hysteresis scans of the samples calcined at 400 °C and 450 °C are presented. The pore size distributions of

the second scans are similar to that of the first scan. The maximum in the pore size distribution is located at 4.9 (Figure 5b) and 5.1 nm (Figure 5d). For the samples calcined at 550 °C, the pore size distribution (Figure 5f) is slightly broader compared to the samples calcined at 400 °C and 450 °C and the maximum in pore size distribution is located at larger pores (around 12 nm). For all three samples, the first three pore size distribution shapes are comparable to each other only with a slight shift towards smaller pores and further first three scans exhibit a hysteresis loop indicating mesopores (IUPAC: type 4 isotherm[65]).

These minor differences show that the pores are not affected by neighboring pores during ad- and desorption process for all presented samples prepared only with citric acid. Additionally, the filling level of the pores is not influencing the desorption behavior of every individual pore, which can be seen in the almost horizontal courses of the desorption branches of all isotherms and the existence of hysteresis in all isotherms. In case of the isotherms of the samples calcined at 400 °C this behavior is best observable for the second scan. Here, the desorption branch of hysteresis of the first scan and the desorption branch of the second scan intersect in the area of the hysteresis of the first scan at 0.48 p/p_0. The isotherms of the different scans further show hysteresis and comparable pore size distributions. Therefore, all isotherms show independent behavior from each other as well as the pores. This is a very important fact for applicability in processes where gases are evolved. The broadening in the pore size distribution in the fourth hysteresis scan of all different samples prepared only with citric acid indicates small amounts of smaller mesopores in the materials. This effect was already investigated on carbon materials.[69] To summarize, the materials synthesized only with citric acid show excellent characteristics of their pore structure for applicability. The pores are independent from each other and gas molecules can desorb completely at every p/p_0 value. The calcination temperature plays no role for the accessibility of the pore network.

Hysteresis scans with the desorption scanning method were also carried out for the materials prepared using citric acid combined with P-123 (Figure S8). The first scan of every sample is again the isotherm with p/p_0 values up to 0.995 (cf. Figure 4).

In this NLDFT data evaluation of the samples calcined at different temperatures (Figure S8b,d,f), it can be observed that the pore size distribution of the 1st and the 2nd scan exhibit almost the same values. The maxima in the pore size distributions are located at 4.9 nm (400 °C), 5.0 nm (450 °C) and 10.5 nm (550 °C). Furthermore, the presence of hysteresis loops in the first and second scan are clearly visible. This shows again that the pores are independent from each other in this p/p_0 region and could be filled and emptied at every p/p_0 value. Still the third scan of every samples has the maximum in pore size distribution comparably to the first and second scan only with a slight broadening towards same smaller mesopores. The fourth scan shows the presence of smaller mesopores more clearly.[69]

The materials synthesized with P-123 and citric acid also exhibit excellent characteristics in the pore structure regarding applicability. The pore characteristics and pore connectivity are
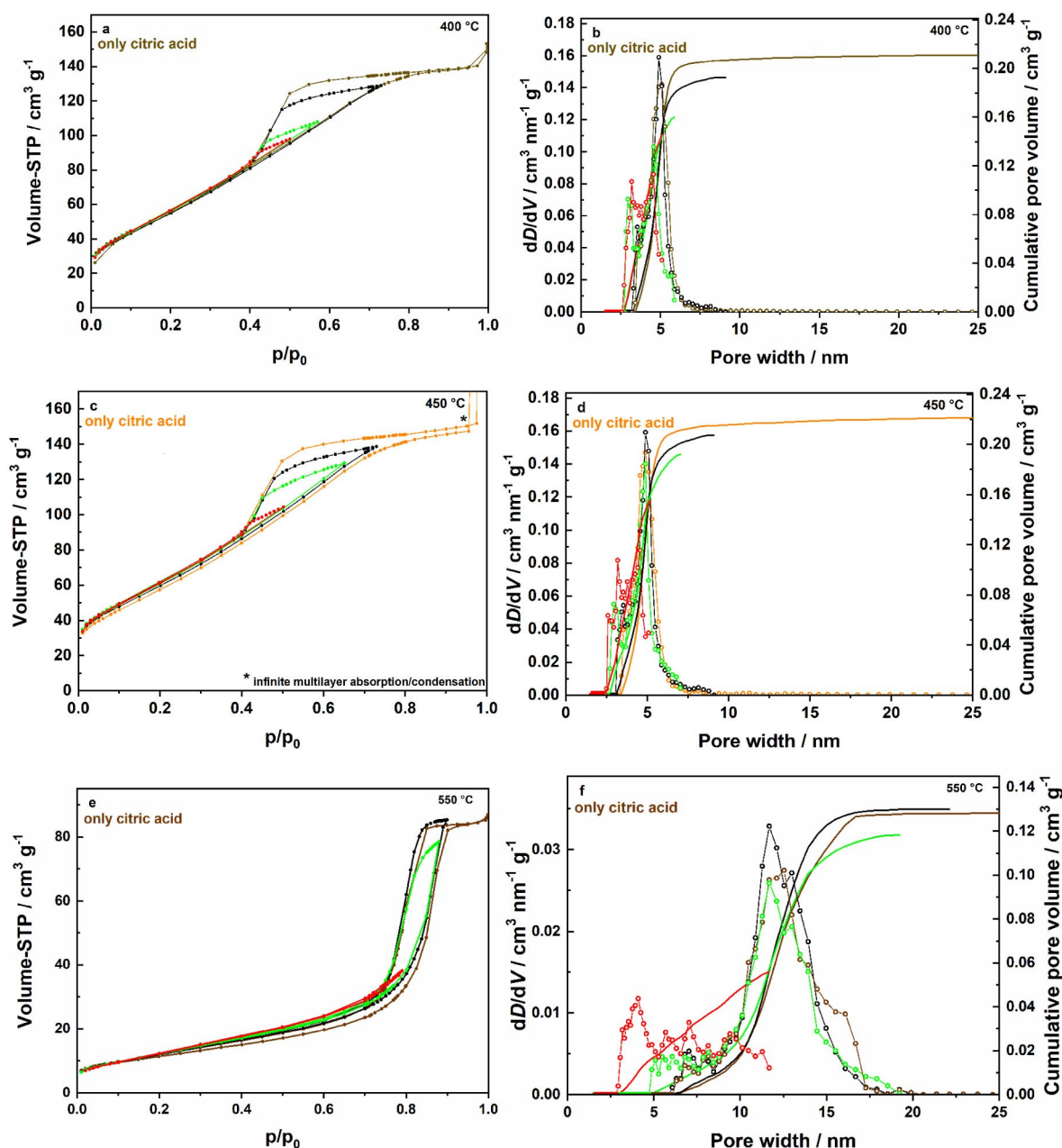
ChemElectroChem

Articles
doi.org/10.1002/celc.202001280

Chemistry
Europe
European Chemical
Societies Publishing

Figure 5. Hysteresis scanning isotherms of mesoporous NiFe₂O₄ samples prepared only with citric acid (a, c, e) and the corresponding pore size distribution plots analyzed by using the NLDFT method (b, d, f). Different scans were indicated with second scan: black, third scan: green and fourth scan: red.

comparable for the samples prepared only with citric acid and with a mixture of citric acid and P-123. Therefore, the detailed analysis of the mesopores of the materials shows the high potential of all prepared materials in application where the pore filling plays a major role, *e.g.* electrocatalytic water splitting.

Concluding all analytical investigations, an overall formation mechanism can be proposed for the presented synthesis strategy. The first step is the complexation of Ni^{2+} and Fe^{3+} cations in aqueous solution by citric acid,[70,71] which is essential for their uniform distribution.[72] Otherwise, cations are distributed unevenly, resulting in the formation of an undesired

hematite by-phase during heat treatment (*cf.* Figure 2). These hybrid structures are conserved during evaporation and drying, respectively. During heat treatment, citric acid metal complexes are converted into amorphous metal carbonate species, *via* several intermediate steps (*cf.* Figure 1). At 275 °C, metal carbonates start to decompose by introducing porosity into the material (*cf.* Figure 1 and Figure 4). Increasing temperature to 400 °C effects the transformation of the amorphous carbonates to the amorphous metal oxide (*cf.* Figure 2b). Investigations on the porosity of the samples (Figure 4) show that the presence of carbonates allows partially removal of organic residues (P-123) before crystal growth of NiFe₂O₄, associated with the

ChemElectroChem

Articles
doi.org/10.1002/celc.202001280

**Chemistry
Europe**
European Chemical
Societies Publishing

formation of thick crystalline pore walls taking place. Highly porous semi-crystalline nickel iron oxides with large surface area and very narrow pore size distribution can be achieved at 450 °C. Moreover, the pores achieved are highly accessible at each pressure, as determined by hysteresis scans (Figure 5 and S8). Through crystallite growth, the generated porous structure of the samples transforms into a particular structure with interparticular voids. Interestingly, the pore size distribution remains relatively narrow even at 550 °C when P-123 and citric acid were used, although TEM images clearly reveal nano-particle agglomerates. Due to detailed investigations on the formation mechanism, phase-pure mesoporous $NiFe_2O_4$ samples with fully accessible pore system were obtained. Apparently, the presence of a block copolymer like P-123 during the initial step of the synthesis does not result in micelle formation. Rather, citric acid and the corresponding carbonates arrange as a scaffold, introducing uniform pores in the materials during thermal removal of organic compounds, whereas the P-123 polymer is able to prevent aggregation of obtained particles during crystallite growth and densification. In Figure S5, X-ray diffraction pattern, Raman spectrum, physisorption isotherm and pore size distribution plot of a 550 °C treated sample prepared without P-123 and without citric acid are shown. The already mentioned presence of the hematite phase shows the need of using citric acid as chelating agent. Further, a loss of pore homogeneity can be observed, since the shape of the isotherm changes significantly and the pore size distribution gets broader compared to the samples prepared with P-123 and citric acid. Larger pores with sizes >20 nm are present, proving the role of P-123 to prevent particle aggregation during densification and crystallite growth even further.

After elucidating the composition and morphology of the samples, we investigated our materials for their applicability in OER electrocatalysis in alkaline media (1 M KOH) using a three-electrode system. A glassy carbon rotating disk electrode modified with $1.4\ mg\ cm^{-2}$ electrocatalyst was applied as working electrode. First, CV measurements were performed to determine the electrochemical surface area (ECSA) of the electrocatalysts (Figure S10). Figure 6a and b display the obtained slopes corresponding to the double layer capacity, which is proportional to the ECSA. The ECSA measurements indicate overall comparable ECSAs for all samples, however the ECSA tends to be higher if samples were calcined at lower temperatures. This trend is in good accordance with the obtained specific surface areas determined via physisorption measurements. However, nickel ferrite synthesized using only citric acid at 550 °C displays a similar value ($C_{DL}=0.73\ mF\ cm^{-2}$) compared to the nickel ferrite with added both P-123 and citric acid ($C_{DL}=0.74\ mF\ cm^{-2}$) while exploiting a specific surface area

smaller by factor 1.6, meaning that a direct correlation between the ECSA and the specific surface area is not generally possible. Interestingly, the sample synthesized using only citric acid at 400 °C displays the smallest values, which contradicts the previously described trend. The reason for this remains elusive. Inaccuracies in the ECSA analysis itself were excluded by performing EIS measurements with the sample with P-123 and citric acid calcined at 400 °C in a non-faradaic region as a representative example. The obtained data was fitted using a Randles circuit including a constant phase element (CPE) (Figure S11). The calculated capacitance using the fit is $0.85\ mF\ cm^{-2}$ which is only slightly higher than the capacitance obtained by CV measurements ($0.81\ mF\ cm^{-2}$). Thus, the EIS data is in good agreement with the data obtained by CV measurements and shows the validity of our data.

The OER performance of the prepared samples was evaluated by performing linear sweep voltammetry experiments (Figure 6c). Samples calcined at 550 °C display a poor activity with a current density of ca. $2.1\ mA\ cm^{-2}$ at 1.7 V. The activity does not increase through the use of P-123 with citric acid with specific surface areas 1.6 times higher, meaning that the ECSA determines the electrochemical activity instead of the specific surface area. Samples calcined at 400 °C or 450 °C display an improved activity, which is influenced by the increased ECSA. In general, crystallinity has only a subordinate role for the activity, since amorphous or semi-crystalline samples calcined at 400 °C or 450 °C exhibit significantly higher current densities. Hence, our results hint that a lower degree of crystallinity by heating at a moderate calcination temperature can be favorable for the overall performance, which agrees with recent literature.[34,73] Hereby, crystallinity and porosity/surface area are coupled directly, since a higher degree of crystallinity implies pore shrinkage or even pore collapse due to crystallite growth. In fact, samples prepared only with citric acid and P-123/citric acid calcined at 400 °C or 450 °C show similar performances in the electrocatalytic water oxidation experiments, which can clearly be correlated to their comparable morphologies. The most active sample, which was prepared only with citric acid and calcined at 400 °C, reaches a current density of $20.8\ mA\ cm^{-2}$ at 1.7 vs. RHE. Overpotentials range from 410 mV to 430 mV, which are acceptable values for OER. In Table 2 the results of the electrochemical measurements are summarized.

Tafel plots of mesoporous $NiFe_2O_4$ samples are shown in Figure 6e and f and display similar Tafel slopes ($50-94\ mV\ dec^{-1}$) compared to other spinel-type electrocatalysts in literature.[30,74] The lower Tafel slopes can probably be correlated to the accessible mesopore systems (cf. Figure 5 and S8), allowing mass transport through our materials, which is often beneficial for transport-related application like electrocatalytic water

Table 2. Results obtained from electrochemical measurements.

	Only citric acid			P-123/citric acid		
	400 °C	450 °C	550 °C	400 °C	450 °C	550 °C
Overpotential for OER [mV]	410	420	>570	420	430	>570
Tafel slope [mV dec^{-1}]	50	51	94	52	55	87
c_{DL} [10^4 F cm^{-2}]	4.53	8.36	7.26	8.14	7.84	7.38

ChemElectroChem

Articles
doi.org/10.1002/celc.202001280

Chemistry Europe
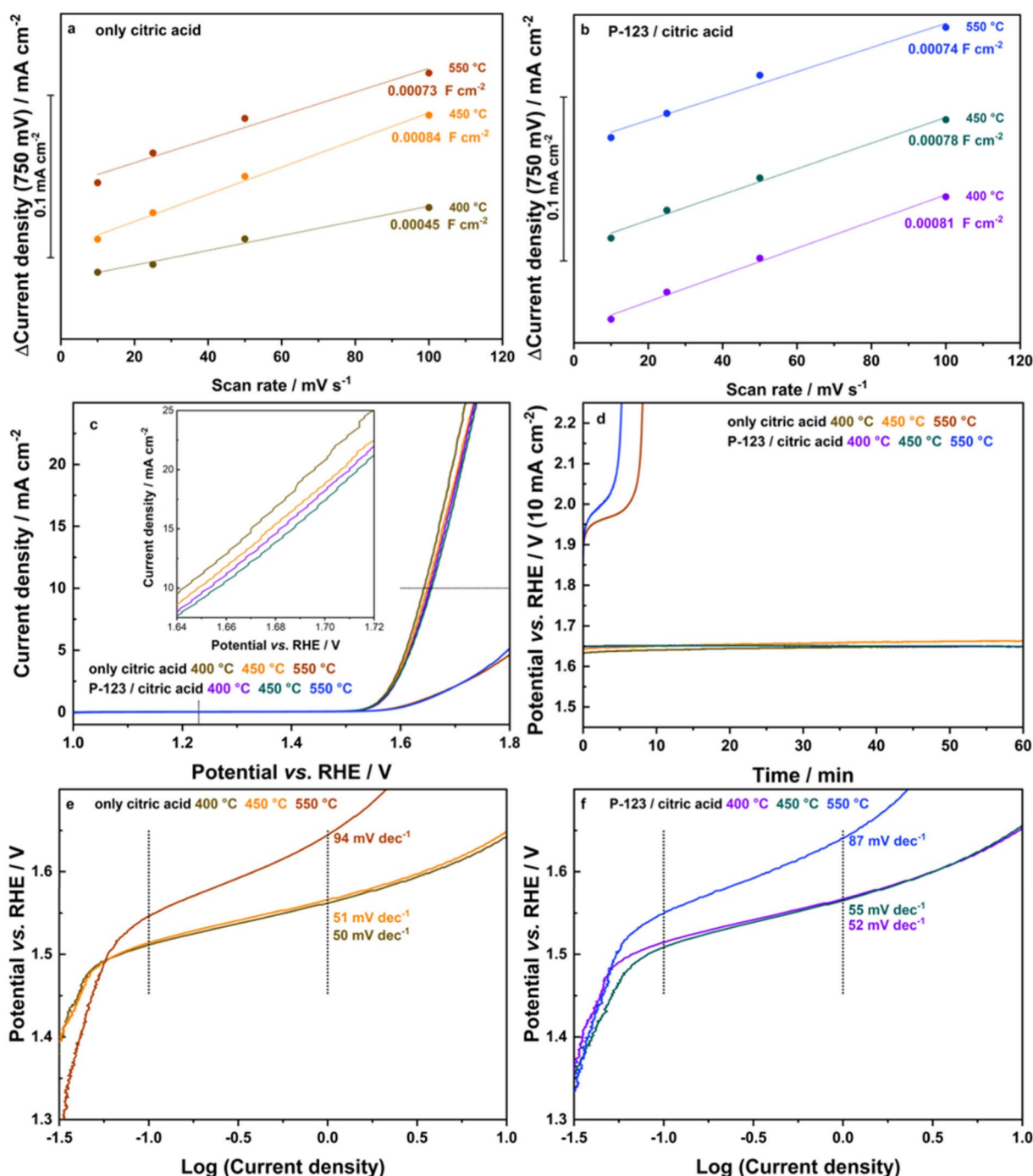European Chemical
Societies Publishing

Figure 6. ECSA slopes determined at 750 mV as a function of the scan rate for the samples prepared only with citric acid (a) and P-123/citric acid combined (b). The linear slope representing the capacitance c_{DL} is proportional to the ECSA. c) Linear sweep voltammograms (LSV) measured with a scan rate of 1 mV s^{-1} in 1 M KOH and d) long-term chronopotentiometric (CPC) stability tests measured for one hour at a constant current density of 10 mA cm^{-2}. Tafel plots of mesoporous NiFe$_2$O$_4$ samples synthesized only with citric acid (e) and P-123/citric acid combined (f).

oxidation. To investigate the long-term stability of the mesoporous materials a constant current density of 10 mA cm^{-2} (chronopotentiometric mode) for the OER was applied (Figure 6d, Figure S12). For all samples calcined at 400 °C and 450 °C, the potential does not change significantly, demonstrating stable performance for at least one hour. In contrast, samples calcined at 550 °C do not steadily catalyze the OER as

the potential increases significantly after approx. 5 minutes. The required high potential for these materials to reach a current density of 10 mA cm^{-2} may lead to corrosion of the glassy carbon surface triggering electrocatalyst detachment of the electrode. The same effect could be observed of the samples calcined at 400 °C and 450 °C but only after approx. 6 h. These additional long-term stability tests in Figure S13 further under-

ChemElectroChem

Articles
doi.org/10.1002/celc.202001280

Chemistry Europe
European Chemical
Societies Publishing

line the assumption of electrocatalyst detachment caused by corrosion of the glassy carbon electrode surface. Electrochemical impedance spectroscopy (EIS) data obtained at 1.6 V *vs.* RHE display the smallest resistance of samples calcined at 450 °C. However, EIS data can be easily misinterpreted and thus leave open, whether the resistances are caused either by altered electrolyte interactions or a minimized charge transfer resistance (Figure S14).

In conclusion, we have demonstrated an altered OER activity depending on the morphology of the synthesized nickel ferrites. In general, high specific surface area materials reveal a trend in increased ECSAs alongside with increased activities. The minimum overpotential reached of 410 mV show the potential of $NiFe_2O_4$ as an electrocatalyst for water oxidation, since previously reported overpotentials for water oxidation with unmodified NiO or Fe_2O_3 are much higher.[56]

3. Conclusions

We present a simple synthesis strategy to prepare phase-pure $NiFe_2O_4$ electrocatalysts with highly accessible mesopores. The materials were prepared by a modified soft-templating strategy using citric acid as scaffold and the optional addition of the commercially available block copolymer Pluronic® P-123, followed by calcination. The formation of intermediate carbonate species induced by the use of citric acid in the synthesis plays a key role in the formation mechanism of the mesoporous structure. Furthermore, citric acid is also crucial to obtain phase-pure $NiFe_2O_4$. The synthesis procedure is easy to handle, low-cost and maybe industrial scalable in the future. Parameters like crystallinity and porosity/surface area can be controlled by the calcination procedure. By keeping the composition constant, the influence of often-neglected parameters like pore homogeneity, pore width, (accessible) surface area, and crystallinity can be investigated precisely. Our results highlight the relation between morphology/crystallinity and performance, demonstrating that high accessible surface areas are essential for high performances, while crystallinity only plays a subordinate role. Hence, the materials can be treated at moderate temperatures, avoiding an energy-consuming heating step at elevated temperatures. Morphological investigations including the hysteresis scanning method can substantially help to fully understand the activity of a nanostructured electrocatalyst. However, the performances of our materials are still limited compared to other $NiFe_2O_4$ nanomaterials like -cubes or -particles[56,75,76] and further to other mixed transition metal oxides.[77] However, our materials are of high purity, while materials described in literature often contain α-Fe_2O_3[76] or NiO,[78] which prevents complete comparability. In contrast to, for example faceted NiFe-oxide nanocubes,[75] controlling the exposed facets in the pore channels is not possible, resulting in a weaker activity of mesoporous $NiFe_2O_4$. More importantly, the incorporated elements are cheap and available, in contrast to cobalt-containing mixed metal oxide electrocatalysts.[79] Long-term stability as another important parameter for application is also provided, contrary to manganese-containing compounds.[80]

Experimental Section

Synthesis

Mesoporous $NiFe_2O_4$ samples were prepared using the well-known EISA process,[81] coupled with the addition of citric acid during the synthesis, inspired by the works of Kraehnert *et al.*[31,43] Therefore, 116.3 mg (0.4 mmol) nickel(II) nitrate hexahydrate (*SigmaAldrich*, 99.999%) were dissolved in 2 mL of deionized water, and stirred for 10 minutes (500 rpm). Afterwards, 323.2 mg (0.8 mmol) iron(III) nitrate nonahydrate (*AcrosOrganics*, 99+%) were added, followed by stirring for 1 hour. Meanwhile, 52.2 mg (0.009 mmol, 0.03 equivalents concerning the Ni precursor) of the commercially available triblock copolymer $PEO_{20}PPO_{70}PEO_{20}$ (Pluronic® P-123, *Sigma-Aldrich*) and 271.1 mg (1.3 mmol, 4.3 equivalents concerning the Ni precursor) citric acid monohydrate (*CarlRoth*, $\geq$ 99,5%) were dissolved in 12 mL of deionized water, and stirred for 1 hour. Then, six portions of 2 mL of polymer and 0.25 mL precursor solutions were each combined. After 2 hours of stirring (500 rpm), the solutions were transferred into 5 mL polytetrafluoroethylene (PTFE) cups, followed by water evaporation under a glass dome at 65 °C on a heating plate for at least 2 days and final drying at 50 °C using a vacuum drying oven. Calcination of the obtained hybrid material was performed at 275 °C/400 °C/450 °C/550 °C for 1 hour in air (heating rate 1 °C/min). For comparison, the synthesis procedure was also performed in the absence of Pluronic® P-123 and/or citric acid, respectively. In the following Pluronic® P-123 will be abbreviated as P-123. Synthesis variations and their labels are summarized in Table S1.

Materials Characterization

Powder X-ray diffraction (PXRD) measurements were performed on a Malvern PANanlytical Empyrean diffractometer with a PixCel 1D detector operating at 40 kV acceleration voltage and 40 mA emission current using Cu K-α radiation (wavelength $\lambda = 1.54060$ Å). For the measurements, the lower level of the pulse-height discrimination (PHD) was set to 8.05 keV, and the upper level to 11.27 keV. Data were recorded in a range from 10–70° 2θ. Crystallite sizes were calculated from the integral width using (220), (400), (511) and (440) reflections of $NiFe_2O_4$. For this purpose, the intensity of the diffraction pattern was plotted versus the scattering vector S (Eq. 1) and the ratio between area and height of an isolated reflex (integral width B_{hkl}) determined. The crystallite size L_{hkl} is then obtained as the inverse value of the integral width B_{hkl}.[82]

$$S = \frac{2 \cdot \sin\left(\frac{\pi}{180°} \cdot \theta\right)}{\lambda} \tag{1}$$

Raman spectra were recorded using a LABRAM I Raman spectrometer from Horiba Jobin Yvon GmbH equipped with an Olympus BX41 microscope using LabSpec 5.78.24 software for data evaluation. For the measurements, a HeNe laser ($\lambda = 632.82$ nm) was used, operated with a laser power of 1.15 mW. Samples were measured at 50x magnification within a range of 100–4000 cm^{-1}, 5 co-additions, and 25 s exposure time. Raman spectra were de-spiked manually and smoothed using a FFT filter, before normalizing the data.

N_2 physisorption analysis were performed at 77 K using an Anton Paar QuantaTec ASiQ-MP-MP-AG instrument (scanning curves) and an Anton Paar QUADRASORB evo surface area & pore size analyzer (standard isotherms). Pore size distributions were calculated using NLDFT equilibrium model assuming cylindrical pores and silica like surface. Specific surface areas were estimated by applying the Brunauer-Emmett-Teller (BET) model. All samples were degassed in

ChemElectroChem

Articles
doi.org/10.1002/celc.202001280

**Chemistry
Europe**
European Chemical
Societies Publishing

vacuum at 120 °C for at least 12 hours prior to the measurements. Data evaluation was carried out with the program ASiQwin 4.0®.

For recording transmission electron microscopy (TEM) images and selected area electron diffraction (SAED) patterns, a 200 kV JEOL JEM-2200FS EFTEM equipped with Schottky FEG and In-Column Omega Energyfilter from JEOL GmbH was used. Prior to each measurement, 1-2 mg of the sample were suspended in 1 mL of ethanol (*AcrosOrganics*, extra dry, 99.5%). Then, 4-8 µL of the suspension were dropped on a carbon film coated Cu TEM grid (200 Mesh). TEM (and also SEM) images were processed using ImageJ 1.52a. Particle sizes were measured from at least 30 independent particles, before averaging the values.

Scanning electron microscopy (SEM) was performed on a Zeiss Leo 1530 instrument at an acceleration voltage of 3.0 kV (working distance 2.5–5 mm). Samples were sputtered with Pt using a Cressington Sputter Coater 208 HR. For the energy-dispersive X-ray spectroscopy (EDXS) experiments, an UltraDry-EDX detector (Thermo Fisher Scientific NS7) was used, while the acceleration voltage was set to 15 kV (working distance 8 mm). For each sample, Ni to Fe ratios were measured at several points, before averaging the values.

For thermogravimetric analysis (TGA), a Netzsch STA409PC thermoscale in combination with a QMG421 quadrupole mass spectrometer from Balzers was utilized. Data were recorded in a range from 30 °C to 800 °C, with a heating rate of 5 °C/min in synthetic air (80% N_2, 20% O_2).

Diffuse reflectance infrared Fourier transform spectroscopy (DRIFTS) data were collected using a Bruker alpha II in a range of 400–4000 cm^{-1} with a spectral resolution of 10 cm^{-1} and 200 co-additions per scan.

^{57}Mössbauer spectra were recorded at room temperature using a ^{57}Co radiation source in a Rh matrix in a SeeCo constant acceleration spectrometer. Isomer shifts are referred to α-Fe metal at room temperature. Data were fit to a single line superposed on a symmetric Hyperfine Field Distribution using a Voigt profile based adaptive least-square routine with the WMOSS program. For the estimation of the inversion degree X, the ratio between the areas under the fits for the two iron sites (tetrahedral, octahedral) was calculated. This ratio is equal to the term $X/(2-X)$.

Electrochemical measurements were performed using a Gamry Interface 1010B or a Gamry Reference 600+ potentiostat. A three-electrode setup was employed utilizing a catalyst modified glassy carbon electrode (GC, diameter 3.0 mm) equipped with an Autolab RDE-2 working, a platinum wire counter and a reversible hydrogen reference electrode (RHE, HydroFlex mini, Gaskatel GmbH). All measured potentials were given against RHE. Catalyst inks were prepared by dispersing 3.3 mg of the catalyst in a 100 µL mixture of water, ethanol and Nafion solution (5% in aliph. alcohols, *Sigma-Aldrich*) in the volume ratio of 8:1:1. Subsequently, the catalyst ink was sonicated for 30 min and a drop of 3 µL (1.4 mg cm^{-2} catalyst loading) was applied to the pre-polished GC electrode surface and was left to dry under air for 30 min. Polishing of the GC electrode was performed with alumina suspensions (0.3 and 0.05 µm, *Buehler*) for 3 min, respectively, followed by ultra-sonication of the GC electrode in Milli-Q water for 5 min.

A 1 M KOH solution (*Fisher Scientific*, 85.3%, used without purification) was used as electrolyte, which was purged with N_2 prior to each electrochemical experiment for 10 min. Linear sweep voltammograms were recorded under N_2 atmosphere with a scan rate of 1 mV s^{-1} and a rotation speed of 1600 rpm. Chronopotentiometry was carried out by applying a constant current of 10 mA cm^{-2} with a rotation speed of 1600 rpm. For evaluation of

electrochemical active surface areas (ECSA), a method presented by McCrory *et al.* was applied.[83] First, cyclic voltammograms were measured in a non-faradaic region (0.65–0.85 V *vs.* RHE) with various scan rates (100, 50, 25, 10 mV s^{-1}). Current density differences of forward and backward scans at 750 mV were plotted against the scan rate. The slope of the resulting linear fit is proportional to the electrochemical double-layer capacitance c_{DL}, and thus proportional to the ECSA. Electrochemical impedance spectroscopy (EIS) measurements were performed at 1.6 V vs. RHE from 100 kz–1 Hz with an amplitude of 1 mV and 10 points per decade.

Conflict of Interest

The authors declare no conflict of interest.

[1] N. H. Chou, P. N. Ross, A. T. Bell, T. D. Tilley, *ChemSusChem* **2011**, *4*, 1566–1569.
[2] A. S. Schenk, S. Eiben, M. Goll, L. Reith, A. N. Kulak, F. C. Meldrum, H. Jeske, C. Wege, S. Ludwigs, *Nanoscale* **2017**, *9*, 6334–6345.
[3] A. Ramírez, P. Hillebrand, D. Stellmach, M. M. May, P. Bogdanoff, S. Fiechter, *J. Phys. Chem. C* **2014**, *118*, 14073–14081.
[4] M. Huynh, C. Shi, S. J. L. Billinge, D. G. Nocera, *J. Am. Chem. Soc.* **2015**, *137*, 14887–14904.
[5] M. E. G. Lyons, R. L. Doyle, *Int. J. Electrochem. Sci.* **2012**, *7*, 9488–9501.
[6] Q. Liu, A. M. Asiri, X. Sun, *Electrochem. Commun.* **2014**, *49*, 21–24.
[7] F. Chekin, H. Tahermansouri, M. R. Besharat, *J. Solid State Electrochem.* **2014**, *18*, 747–753.
[8] J. C. B. Nadesan, A. C. C. Tseung, *J. Electrochem. Soc.* **1985**, *132*, 2957–2959.
[9] A. Kargar, S. Yavuz, T. K. Kim, C. H. Liu, C. Kuru, C. S. Rustomji, S. Jin, P. R. Bandaru, *ACS Appl. Mater. Interfaces* **2015**, *7*, 17851–17856.
[10] X. Lv, Y. Zhu, H. Jiang, X. Yang, Y. Liu, Y. Su, J. Huang, Y. Yao, C. Li, *Dalton Trans.* **2015**, *44*, 4148–4154.
[11] X. Kong, T. Zhu, F. Cheng, M. Zhu, X. Cao, S. Liang, G. Cao, A. Pan, *ACS Appl. Mater. Interfaces* **2018**, *10*, 8730–8738.
[12] X. F. Lu, L. F. Gu, J. W. Wang, J. X. Wu, P. Q. Liao, G. R. Li, *Adv. Mater.* **2017**, *29*, 1604437.

[13] G. Liu, K. Wang, X. Gao, D. He, J. Li, *Electrochim. Acta* **2016**, *211*, 871–878.

[14] Q. Qin, L. Chen, T. Wei, Y. Wang, X. Liu, *Catal. Sci. Technol.* **2019**, *9*, 1595–1601.

[15] M. Li, Y. Xiong, X. Liu, X. Bo, Y. Zhang, C. Han, L. Guo, *Nanoscale* **2015**, *7*, 8920–8930.

[16] A. Sutka, M. Kodu, R. Pärna, R. Saar, I. Juhnevica, R. Jaaniso, V. Kisand, *Sens. Actuators B* **2016**, *224*, 260–265.

[17] J. Wu, D. Gao, T. Sun, J. Bi, Y. Zhao, Z. Ning, G. Fan, Z. Xie, *Sens. Actuators B* **2016**, *235*, 258–262.

[18] K. Kirchberg, R. Marschall, *Sustain. Energy Fuels* **2019**, *3*, 1150–1153.

[19] S. Ida, K. Yamada, T. Matsunaga, H. Hagiwara, Y. Matsumoto, T. Ishihara, *J. Am. Chem. Soc.* **2010**, *132*, 17343–17345.

[20] T. Peng, X. Zhang, H. Lv, L. Zan, *Catal. Commun.* **2012**, *28*, 116–119.

[21] D. Tetzlaff, C. Simon, D. S. Achilleos, M. Smialkowski, K. junge Puring, A. Bloesser, S. Piontek, H. Kasap, D. Siegmund, E. Reisner, et al., *Faraday Discuss.* **2019**, 216–226.

[22] K. Kirchberg, S. Wang, L. Wang, R. Marschall, *ChemPhysChem* **2018**, *19*, 2313–2320.

[23] N. Guijarro, P. Bornoz, M. S. Prévot, X. Yu, X. Zhu, M. Johnson, X. A. Jeanbourquin, F. Le Formal, K. Sivula, *Sustain. Energy Fuels* **2017**, *2*, 103–117.

[24] A. G. Hufnagel, K. Peters, A. Müller, C. Scheu, D. Fattakhova-Rohlfing, T. Bein, *Adv. Funct. Mater.* **2016**, *26*, 4435–4443.

[25] L. I. Granone, A. C. Ulpe, L. Robben, S. Klimke, M. Jahns, F. Renz, T. M. Gesing, R. Bredow, D. Dillert, D. W. Bahnemann, *Phys. Chem. Chem. Phys.* **2018**, *20*, 28267–28278.

[26] D. Peeters, D. H. Taffa, M. M. Kerrigan, A. Ney, N. Jöns, D. Rogalla, S. Cwik, H. W. Becker, M. Grafen, A. Ostendorf, et al., *ACS Sustainable Chem. Eng.* **2017**, *5*, 2917–2926.

[27] K. Kirchberg, A. Becker, A. Bloesser, T. Weller, J. Timm, C. Suchomski, R. Marschall, *J. Phys. Chem. C* **2017**, *121*, 27126–27138.

[28] R. Galindo, E. Mazario, S. Gutiérrez, M. P. Morales, P. Herrasti, *J. Alloys Compd.* **2012**, *536*, S241–S244.

[29] Z. Wu, Z. Zou, J. Huang, F. Gao, *ACS Appl. Mater. Interfaces* **2018**, *10*, 26283–26292.

[30] N. K. Singh, R. N. Singh, *Indian J. Chem. Sect. A* **1999**, *38 A*, 491–495.

[31] M. Bernicke, B. Eckhardt, A. Lippitz, E. Ortel, D. Bernsmeier, R. Schmack, R. Kraehnert, *ChemistrySelect* **2016**, *1*, 482–489.

[32] N. Menzel, E. Ortel, R. Kraehnert, P. Strasser, *ChemPhysChem* **2012**, *13*, 1385–1394.

[33] F. J. Keil, *Catal. Today* **1999**, *53*, 245–258.

[34] T. Priamushko, R. Guillet-Nicolas, M. Yu, M. Doyle, C. Weidenthaler, H. Tüysüz, F. Kleitz, *ACS Appl. Mater. Interfaces* **2020**, *3*, 5597–5609.

[35] G. Ou, F. Wu, K. Huang, N. Hussain, D. Zu, H. Wei, B. Ge, H. Yao, L. Liu, H. Li, et al., *ACS Appl. Mater. Interfaces* **2019**, *11*, 3978–3983.

[36] Q. Chen, R. Wang, F. Lu, X. Kuang, Y. Tong, X. Lu, *ACS Omega* **2019**, *4*, 3493–3499.

[37] A. Thomas, H. Schlaad, B. Smarsly, M. Antonietti, *Langmuir* **2003**, *19*, 4455–4459.

[38] J. Haetge, C. Suchomski, T. Brezesinski, *Inorg. Chem.* **2010**, *49*, 11619–11626.

[39] C. Jia, Y. Zhang, Q. Kong, Q. Wang, G. Chen, H. T. Guam, C. Dong, *J. Mater. Sci. Mater. Electron.* **2020**, *31*, 6000–6007.

[40] X. Gu, W. Zhu, C. Jia, R. Zhao, W. Schmidt, Y. Wang, *Chem. Commun.* **2011**, *47*, 5337.

[41] Y. Li, K. Guo, J. Li, X. Dong, T. Yuan, X. Li, H. Yang, *ACS Appl. Mater. Interfaces* **2014**, *6*, 20949–20957.

[42] H. Yen, **n.d.**

[43] B. Eckhardt, E. Ortel, D. Bernsmeier, J. Polte, P. Strasser, U. Vainio, F. Emmerling, R. Kraehnert, *Chem. Mater.* **2013**, *25*, 2749–2758.

[44] W. Brockner, C. Ehrhardt, M. Gjikaj, *Thermochim. Acta* **2007**, *456*, 64–68.

[45] P. Melnikov, V. A. Nascimento, I. V. Arkhangelsky, L. Z. Zanoni Consolo, L. C. S. De Oliveira, *J. Therm. Anal. Calorim.* **2014**, *115*, 145–151.

[46] S. Mehrabani, J. P. Singh, R. Bagheri, A. G. Wattoo, Z. Song, K. H. Chae, M. M. Najafpour, *Nanoscale Adv.* **2019**, *1*, 686–695.

[47] D. Esken, H. Noei, Y. Wang, C. Wiktor, S. Turner, G. Van Tendeloo, R. A. Fischer, *J. Mater. Chem.* **2011**, *21*, 5907–5915.

[48] X. Wang, L. Andrews, *J. Phys. Chem. A* **2006**, *110*, 10035–10045.

[49] J. P. Gallas, J. M. Goupil, A. Vimont, J. C. Lavalley, B. Gil, J. P. Gilson, O. Miserque, *Langmuir* **2009**, *25*, 5825–5834.

[50] M. Ide, M. El-Roz, E. De Canck, A. Vicente, T. Planckaert, T. Bogaerts, I. Van Driessche, F. Lynen, V. Van Speybroeck, F. Thybault-Starzyk, et al., *Phys. Chem. Chem. Phys.* **2013**, *15*, 642–650.

[51] K. V. P. M. Shafi, Y. Koltypin, A. Gedanken, R. Prozorov, J. Balogh, J. Lendvai, I. Felner, *J. Phys. Chem. B* **1997**, *101*, 6409–6414.

[52] M. Zainuri, *IOP Conf. Ser.: Mater. Sci. Eng.* **2017**, *196*, 1–4.

[53] K. K. Lee, Y. C. Kang, K. Y. Jung, J. H. Kim, *J. Alloys Compd.* **2005**, *395*, 280–285.

[54] W. B. White, B. A. DeAngelis, *Spectrochim. Acta Part A* **1967**, *23*, 985–995.

[55] A. Ahlawat, V. G. Sathe, *J. Raman Spectrosc.* **2011**, *42*, 1087–1094.

[56] N. Dalai, B. Mohanty, A. Mitra, B. Jena, *ChemistrySelect* **2019**, *4*, 7791–7796.

[57] P. R. Graves, C. Johnston, J. J. Campaniello, *Mater. Res. Bull.* **1988**, *23*, 1651–1660.

[58] D. L. A. de Faria, S. Venâncio Silva, M. T. de Oliveira, *J. Raman Spectrosc.* **1997**, *28*, 873–878.

[59] V. Bartůněk, D. Sedmidubský, Š. Huber, P. Ulbrich, O. Jankovský, *Materials* **2018**, *10*, 1–11.

[60] C. Zhao, H. Li, J. Jiang, Y. He, W. Liang, *High Press. Res.* **2018**, *38*, 212–223.

[61] E. De Grave, A. Govaert, D. Chambaere, G. Robbrecht, *Physica B + C* **1979**, *96*, 103–110.

[62] E. Greenberg, W. M. Xu, M. Nikolaevsky, E. Bykova, G. Garbarino, K. Glazyrin, D. G. Merkel, L. Dubrovinsky, M. P. Pasternak, G. K. Rozenberg, *Phys. Rev. B* **2017**, *95*, 1–13.

[63] E. Agouriane, A. Essoumhi, A. Razouk, M. Sahlaoui, M. Sajieddine, *J. Mater. Environ. Sci.* **2016**, *7*, 4614–4619.

[64] H. S. C. O'Neill, H. Annersten, D. Virgo, *Am. Mineral.* **1992**, *77*, 725–740.

[65] M. Thommes, K. Kaneko, A. V. Neimark, J. P. Olivier, F. Rodriguez-Reinoso, J. Rouquerol, K. S. W. Sing, *Pure Appl. Chem.* **2015**, *87*, 1051–1069.

[66] J. Jeromenok, J. Weber, *Langmuir* **2013**, *29*, 12982–12989.

[67] K. A. Cychosz, R. Guillet-Nicolas, J. García-Martínez, M. Thommes, *Chem. Soc. Rev.* **2017**, *46*, 389–414.

[68] R. Cimino, K. A. Cychosz, M. Thommes, A. V. Neimark, *Colloids Surf. A* **2013**, *437*, 76–89.

[69] K. A. Cychosz, X. Guo, W. Fan, R. Cimino, G. Y. Gor, M. Tsapatsis, A. V. Neimark, M. Thommes, *Langmuir* **2012**, *28*, 12647–12654.

[70] G. R. Hedwig, J. R. Liddle, R. D. Reeves, *Aust. J. Chem.* **1980**, *33*, 1685–1693.

[71] C. F. Timberlake, *J. Chem. Soc.* **1964**, 5078–5085.

[72] A. E. Danks, S. R. Hall, Z. Schnepp, *Mater. Horiz.* **2016**, *3*, 91–112.

[73] S. S. Nkabinde, Z. B. Ndala, N. P. Shumbula, T. Kolokoto, O. Nchoe, G. N. Ngubeni, K. P. Mubiayi, N. Moloto, *New J. Chem.* **2020**, *44*, 14041–14049.

[74] K. Chakrapani, G. Bendt, H. Hajiyani, I. Schwarzrock, T. Lunkenbein, S. Salamon, J. Landers, H. Wende, R. Schlögl, R. Pentcheva, et al., *ChemCatChem* **2017**, *9*, 2988–2995.

[75] A. Kumar, S. Bhattacharyya, *ACS Appl. Mater. Interfaces* **2017**, *9*, 41906–41915.

[76] D. Lim, H. Kong, N. Kim, C. Lim, W. S. Ahn, S. H. Baeck, *ChemNanoMat* **2019**, *5*, 1296–1302.

[77] Z. P. Wu, X. F. Lu, S. Q. Zang, X. W. Lou, *Adv. Funct. Mater.* **2020**, *30*, 1–20.

[78] B. K. Kang, M. H. Woo, J. Lee, Y. H. Song, Z. Wang, Y. Guo, Y. Yamauchi, J. H. Kim, B. Lim, D. H. Yoon, *J. Mater. Chem. A* **2017**, *5*, 4320–4324.

[79] V. Maruthapandian, M. Mathankumar, V. Saraswathy, B. Subramanian, S. Muralidharan, *ACS Appl. Mater. Interfaces* **2017**, *9*, 13132–13141.

[80] F. D. Speck, P. G. Santori, F. Jaouen, S. Cherevko, *J. Phys. Chem. C* **2019**, *123*, 25267–25277.

[81] T. Weller, L. Deilmann, J. Timm, T. S. Dörr, P. A. Beaucage, A. S. Cherevan, U. B. Wiesner, D. Eder, R. Marschall, *Nanoscale* **2018**, *10*, 3225–3234.

[82] H. G. Jiang, M. Rühle, E. J. Lavernia, *J. Mater. Res.* **1999**, *14*, 549–559.

[83] C. C. L. McCrory, S. Jung, J. C. Peters, T. F. Jaramillo, *J. Am. Chem. Soc.* **2013**, *135*, 16977–16987.